

Effect of Surface Fluxes versus Radiative Cooling on Tropical Deep Convection.

Usama Anber^{1,3}, Shuguang Wang², and Adam Sobel^{1,2,3}

1 Lamont-Doherty Earth Observatory of Columbia University, Palisades,
NY

2 Department of Applied Physics and Applied Mathematics, Columbia
University, New York, NY

3 Department of Earth and Environmental Sciences, Columbia University,
New York, NY

1

Corresponding Author: Usama Anber, Lamont-Doherty Earth Observatory, 61 Route 9W,
Palisades, NY 10964. E-mail: uanber@ldeo.columbia.edu

2 ABSTRACT

3 The effects of turbulent surface fluxes and radiative cooling on tropical deep
4 convection are compared in a series of idealized cloud-system resolving simulations with
5 parameterized large scale dynamics. Two methods of parameterizing the large scale
6 dynamics are used; the Weak Temperature Gradient (WTG) approximation and the
7 Damped Gravity Wave (DGW) method. Both surface fluxes and radiative cooling are
8 specified, with radiative cooling taken constant in the vertical in the troposphere. All
9 simulations are run to statistical equilibrium.

10 In the precipitating equilibria, which result from sufficiently moist initial
11 conditions, an increment in surface fluxes produces more precipitation than equal
12 increment of column-integrated radiative cooling. This is straightforwardly understood in
13 terms of the column-integrated moist static energy budget with constant normalized gross
14 moist stability. Under both large-scale parameterizations, the gross moist stability does in
15 fact remain close to constant over a wide range of forcings, and the small variations
16 which occur are similar for equal increments of surface flux and radiative heating.

17 With completely dry initial conditions, the WTG simulations exhibit hysteresis,
18 maintaining a dry state with no precipitation for a wide range of net energy inputs to the
19 atmospheric column. The same boundary conditions and forcings admit a rainy state also
20 (for moist initial conditions), and thus multiple equilibria exist under WTG. When the net
21 forcing (surface fluxes minus radiative cooling) is increased enough that simulations
22 which begin dry eventually develop precipitation, the dry state persists longer after
23 initialization when the surface fluxes are increased than when radiative cooling is

24 decreased. The DGW method, however, shows no multiple equilibria in any of the
25 simulations.

26 **1. Introduction**

27 Surface turbulent heat fluxes and electromagnetic radiation are the most important
28 sources of moist static energy (or moist entropy) to the atmosphere. In the idealized state
29 of radiative-convective equilibrium (RCE), the source due to surface fluxes must balance
30 the sink due to radiative cooling. In this state, the surface evaporation and precipitation
31 also balance, and there is no large-scale circulation. In a more realistic situation in which
32 there is a large-scale circulation, the strength of that circulation's horizontally divergent
33 component can be viewed as proportional, in a column-integrated sense, to the net moist
34 static energy source (surface fluxes minus column-integrated radiative cooling), with the
35 proportionality factor being known as the gross moist stability.

36 There is no accepted theory which satisfactorily predicts the gross moist stability.
37 It is itself a function of the large-scale circulation, and may be dynamically varying. If
38 we could be certain that it would remain constant, however, then not only would the
39 divergent circulation (i.e., the large-scale vertical motion) be predictable as a function of
40 the surface fluxes and radiative cooling, but surface fluxes and radiative cooling would
41 influence that circulation in the same way. All that would matter would be the difference
42 between the two, the column-integrated net moist static energy forcing. This study
43 investigates, in an idealized setting, whether this is the case. We ask whether surface
44 fluxes and radiation influence the circulation differently. We might expect that they
45 would, given that surface fluxes act at the surface while radiation acts throughout the
46 column. Such a difference would necessarily be expressed (at least in the time mean) as

47 a difference in the gross moist stability between two situations in which the net moist
48 static energy source is the same, but its partitioning between surface fluxes and radiation
49 is different.

50 We study this problem using a Cloud Resolving Model (CRM). CRMs have
51 proven to be very powerful tools for studying deep moist convection. One set of useful
52 studies involves simulations of RCE (e.g., Emanuel 2007, Robe and Emanuel 2001,
53 Tompkins and Craig 1998a, Bretherton et al. 2005, Muller and Held 2012, Popke et al.
54 2012, Wing and Emanuel 2014). While RCE has provided many useful insights, it
55 entirely neglects the influences of the large scale circulation. Another approach is to
56 parameterize the large scale circulation (e.g., Sobel and Bretherton 2000; Mapes 2004;
57 Bergman and Sardeshmukh 2004; Raymond and Zeng 2005; Kuang 2011; Romps 2012;
58 Wang and Sobel 2011; Anber et al. 2014; Edman and Romps 2014) as a function of
59 variables resolved within a small domain. This approach is computationally inexpensive
60 (compared to using domains large enough to resolve the large scales present on the real
61 earth), and provides a two-way interaction between cumulus convection and large scale
62 dynamics .

63

64 One method to parameterize the large scale dynamics is called the Weak
65 Temperature Gradient (WTG) approximation (Sobel and Bretherton 2000). As the name
66 suggests, this method relies explicitly on the smallness of the temperature gradient in the
67 tropics, which is a consequence of the small Coriolis parameter there. Any temperature,
68 or density, anomaly in the free troposphere generated by diabatic processes is rapidly
69 wiped out by means of gravity wave adjustment to restore the temperature profile to that

70 of the adjacent regions. Hence the dominant balance is between diabatic heating and
71 adiabatic cooling, and the tropospheric temperature is constrained to remain close to a
72 target profile which is interpreted as that of surrounding regions.

73 While WTG captures the net result of the gravitational adjustment, it does not
74 simulate the gravity waves themselves. Another method of representing the large scale
75 dynamics in CRMs represents those dynamics as resulting explicitly from such waves,
76 with a single wavenumber, interacting with the simulated convection. This method was
77 introduced by Kuang (2008) and Blossey et al. (2009) and is called the Damped Gravity
78 Wave (DGW) method.

79 Both methods have been shown to produce results qualitatively similar to
80 observations in some settings; for example, Wang et al. (2013) compared the two
81 methods with observations produced during the TOGA-COARE field experiment.
82 Utilizing both of the above two methods, as we do here, allows us to explore a variety of
83 mechanisms and parameters affecting the interaction between deep convection and large
84 scale dynamics, among which are the surface turbulent fluxes and radiative cooling.

85 In numerical experiments using the WTG method, Sobel et al. (2007) and
86 Sessions et al. (2010) found that the statistically steady solution is not unique for some
87 forcings: the final solutions can be almost entirely dry, with zero precipitation, or rainy,
88 depending on the initial moisture content. We have interpreted this behavior as relevant
89 to the phenomenon of “self-aggregation” in large-domain RCE simulations (Bretherton et
90 al. 2005; Muller and Held; Wing and Emanuel 2014), with the two states corresponding
91 to dry and rainy regions within the large domain. Tobin et al. (2012) find evidence of this
92 behavior in observations. In the present study, we perform sets of simulations with

93 different initial conditions to look for multiple equilibria, and to determine whether their
94 existence or persistence is influenced differently by surface fluxes and radiation.

95 This paper is organized as follows: in section 2 we describe the model and the
96 experiment setup. In section 3 we show results. We highlight some implications of our
97 results and conclude in section 4.

98

99 **2. Model configuration and experimental setup:**

100 *2.1. Model configuration:*

101 We use the Weather Research and Forecast (WRF) model version 3.3, in three
102 spatial dimensions, with doubly periodic lateral boundary conditions. The experiments
103 are conducted with Coriolis parameter $f=0$. The domain size is $192 \times 192 \text{ km}^2$, with a
104 horizontal grid spacing of 2 km. There are 50 vertical levels in the domain, extending to
105 22 km high, with 10 levels in the lowest 1 km. Gravity waves propagating vertically are
106 absorbed in the top 5 km to prevent unphysical wave reflection off the top boundary
107 using the implicit damping vertical velocity scheme (Klemp et al. 2008). The 2-
108 dimensional Smagorinsky first-order closure scheme is used to parameterize the
109 horizontal transports by sub-grid scale eddies. The Yonsei University (YSU) first order
110 closure scheme is used to parameterize boundary layer turbulence and vertical subgrid
111 scale eddy diffusion (Hong and Pan 1996; Noh et al. 2003; Hong et al. 2006). The
112 microphysics scheme is the Purdue-Lin bulk scheme (Lin et al. 1983; Rutledge and
113 Hobbs 1984; Chen and Sun 2002) that has six species: water vapor, cloud water, cloud
114 ice, rain, snow, and graupel.

115 We first perform an RCE experiment at fixed sea surface temperature of 28 °C
 116 until equilibrium is reached at about 60 days. Results from this experiment are averaged
 117 over the last 10 days to obtain statistically equilibrated temperature and moisture profiles.
 118 Figure 1 shows the resulting vertical profiles of (a) temperature and (b) moisture. These
 119 profiles are then used to initialize other runs with parameterized large scale circulations,
 120 and the temperature profile is used as the target profile against which perturbations are
 121 computed in both the WTG and DGW methods. We will call the RCE moisture profile
 122 the non-zero moisture profile, or wet conditions, to distinguish it from other moisture
 123 profiles (zero, in particular, or dry conditions) used in this paper.

124

125 *2.2. Parameterized large scale circulation:*

126 The large scale vertical velocity is dynamically determined using either the WTG
 127 or the DGW method. In the relaxed form of WTG used in CRM simulation (Raymond
 128 and Zeng 2005; Wang and Sobel 2010; Wang et al. 2013; Anber et al. 2014) the vertical
 129 velocity W is obtained by:

130

$$131 \quad W(z) = \begin{cases} \frac{1}{\tau} \frac{\theta - \theta_0}{\partial \theta / \partial z} & ; z \geq h \\ \frac{z}{h} W(h) & ; z < h \end{cases} \quad \dots(1)$$

132

133 where θ is the domain mean potential temperature, θ_0 is the reference temperature (from
 134 RCE run), h is the height of the boundary layer determined internally by the boundary

135 layer scheme, and τ is the relaxation time scale, and can be thought of as the time scale
136 over which gravity waves propagate out of the domain, taken here 3 hours.

137

138 In DGW method (Kuang 2008; Blossey et al 2009; Romps 2012a, 2012b; Wang
139 et al. 2013) the large scale vertical velocity is obtained by solving the elliptic partial
140 differential equation:

141

$$142 \quad \frac{\partial}{\partial p} \left(\varepsilon \frac{\partial \omega}{\partial p} \right) = \frac{k^2 R_d}{p} (T_v - T_v^0) \quad \dots(2)$$

143 where p the pressure, ω is the pressure vertical velocity, R_d is the dry gas constant, T_v is
144 the domain mean virtual temperature, T_v^0 is the target virtual temperature (from RCE), ε
145 is the momentum damping, in general a function of pressure but here taken constant at
146 1 day^{-1} , and k is the wavenumber taken $1.6 \times 10^{-5} \text{ m}^{-1}$.

147 The boundary conditions used for solving (2) are:

148

$$149 \quad \omega(0) = \omega(100 \text{ hpa}) = 0$$

150

151 Once the vertical velocity obtained from (1) or (2), it is used to vertically advect domain
152 mean temperature and moisture at each time step. Horizontal moisture advection is not
153 represented.

154 The free parameters used here are chosen to give a reasonable comparison between the
155 general characteristics of the two methods, and to produce a close, but not exact,
156 precipitation magnitude in the control runs.

157

158

159 *2.3. Experiment design*

160 All simulations are conducted with prescribed surface fluxes and radiative cooling
161 and no mean wind. Radiative cooling is set to a constant rate in the troposphere, while the
162 stratospheric temperature is relaxed towards 200 K over 5 days as in Wang and Sobel
163 (2011) and Anber et al. (2014).

164 The control runs have surface fluxes of 205 Wm^{-2} ; latent heat flux (LH) of 186 Wm^{-2} and
165 sensible heat flux (SH) of 19 Wm^{-2} , (the ratio of the two corresponding to Bowen ratio of
166 0.1) and vertically integrated radiative cooling of 145 Wm^{-2} , corresponding to a radiative
167 heating rate of -1.5 K/day in the troposphere in both the WTG and DGW experiments.

168 (Note that we use both the terms “radiative cooling” and “radiative heating” although one
169 is simply the negative of the other. The radiative heating is always negative in our
170 simulations and thus is most simply described as “radiative cooling”, but when we
171 compare different simulations a positive change – an increase in radiative heating – is
172 directly compared to a positive change in surface turbulent heat fluxes, and thus when
173 such changes are described it is simpler to describe such changes in terms of radiative
174 heating.)

175 We perform two sets of experiments with parameterized large scale dynamics:
176 one in which surface fluxes are varied by increasing or decreasing their prescribed
177 magnitude by 20 Wm^{-2} from the control run while holding radiative cooling fixed at 145
178 Wm^{-2} , and the other in which the prescribed radiative cooling is varied in increments of
179 20 Wm^{-2} while holding surface fluxes fixed. Perturbations in $\langle Q_R \rangle$ are performed by

180 varying radiative cooling rate while holding in uniform in the vertical. Table 1
181 summarizes the control parameters of the numerical experiments.

182 Another two sets of simulations (with two methods) are performed which are
183 identical except that they are initialized with zero moisture profile (or “dry conditions”).
184 All mean quantities are plotted as a function of the net energy input (NEI) to the
185 atmospheric column excluding the contribution from circulation. Thus, NEI is the sum of
186 surface fluxes (SF) and vertically integrated radiative heating ($\langle Q_R \rangle$): $NEI = SF + \langle Q_R \rangle$.

187

188 **3. Results:**

189 **3.1. Precipitation and Normalized Gross Moist Stability**

190 *a. Mean precipitation:*

191 *a.1. Non-zero initial moisture conditions:*

192 Figure 2 shows the domain and time mean precipitation as a function of the net
193 energy input (NEI) using the non-zero moisture profile as initial condition with (a) WTG
194 and (b) DGW. At zero NEI, in one set of (red) experiments the radiative cooling rate is
195 reduced from that in the control to balance surface fluxes (205 Wm^{-2}); while in the other
196 (blue) surface fluxes is reduced to balance radiative cooling (145 Wm^{-2}). The former
197 gives more precipitation in both WTG and DGW experiments.

198 In all these experiments, the precipitation rate varies linearly over a broad range
199 of NEI values. The precipitation rate produced for a given increment of surface fluxes
200 exceeds that produced for the same increment of vertically integrated radiative heating
201 (equivalently, the opposite increment in radiative cooling). For example, increasing
202 surface fluxes by 40 Wm^{-2} from the control run (i.e. at 100 Wm^{-2} or surface fluxes

203 exceeds radiative cooling by 100 Wm^{-2}) there is more precipitation (blue curve) than if
 204 we decrease radiative cooling by 40 Wm^{-2} (red curve).

205

206 It is straightforward to understand this difference in the slopes of precipitation
 207 responses from the point of view of the column-integrated moist static energy budget. We
 208 use the steady state diagnostic equation for precipitation as in, e.g., Sobel (2007), Wang
 209 and Sobel (2011), or Raymond et al. (2009):

210
$$P = \frac{1}{M}(L + H + \langle Q_R \rangle) - \langle Q_R \rangle - H \quad \dots(3)$$

211 Where $\langle . \rangle = \int_{P_0}^{P_T} dp/g$ is the mass weighted vertical integral from the bottom to the top
 212 of the domain. P , L , H , SF and Q_R are precipitation, latent heat flux, sensible heat flux,
 213 surface fluxes (sum of latent and sensible heat flux), and radiative heating.

214 We define $M = \left\langle W \frac{\partial \bar{h}}{\partial z} \right\rangle / \left\langle W \frac{\partial \bar{s}}{\partial z} \right\rangle$ as the normalized gross moist stability, which
 215 represents the export of moist static energy by the large-scale circulation per unit of dry
 216 static energy export (e.g., Neelin and Held 1987; Sobel 2007; Raymond et al. 2009;
 217 Wang and Sobel 2011; Anber et al 2014). Here h is the moist static energy (sum of the
 218 thermal, potential and latent energy), s is the dry static energy (thermal and potential
 219 energy), and the overbar is the domain mean and time mean.

220 The second and third terms (combined) on the right hand side of (3) represent the
 221 precipitation that would occur in radiative convective equilibrium. The first term
 222 accounts for the contribution by the large scale circulation, which arises from the
 223 discrepancy between surface fluxes and vertically integrated radiative cooling. Therefore,

224 $\langle Q_R \rangle$ contributes to P in two ways with opposite signs; to the dynamic part (the first term
225 on the right hand side of (3)), similar to the contribution from surface fluxes, and to the
226 RCE precipitation (the second term on the RHS of (3)) in an opposite sense. Surface
227 fluxes, on the other hand, contribute only positively.

228 Figure 3 shows the normalized gross moist stability (M) as a function of $NEI > 0$
229 for cases initialized with non-zero initial moisture conditions from (a) WTG and (b)
230 DGW experiments. M is a positive number less than 1 and remains close to constant
231 under each forcing method, though the values under DGW are consistently smaller than
232 those under WTG. The smallness of the variations in M is a nontrivial result; we know no
233 *a priori* reason why M could not vary more widely. Even the variations which do occur
234 as a function of NEI are similar for equal increments of surface flux or radiative heating,
235 over most of the range, particularly in DGW. The most marked differences occur at NEI
236 $= 20 \text{ Wm}^{-2}$ under WTG, the value closest to RCE.

237 At $NEI = 0$ the large scale vertical velocity vanishes and M is undefined; however
238 M in that case is not needed to compute P . Equation (3) is derived by eliminating the
239 vertical advection term between the moist and dry static energy equations, but $NEI = 0$
240 corresponds to RCE, in which the vertical advection vanishes. In that case, the
241 precipitation is simply $P = -\langle Q_R \rangle - H$.

242 When there is a large-scale circulation such that (3) is valid, we can see that if M
243 and the surface fluxes are held fixed, the change in precipitation per change in radiative
244 cooling is:

245
$$\frac{\partial P}{\partial \langle Q_R \rangle} = \frac{1}{M} - 1 \quad \dots(4).$$

246 As discussed above, Figure 3 shows that constancy of M is a good approximation for all
 247 the numerical experiments.

248 On the other hand, the change in precipitation due to an increment in surface fluxes
 249 (holding radiative cooling and M fixed) scales as:

250
$$\frac{\partial P}{\partial SF} = \frac{1}{M} \quad \dots(5).$$

251 Equations (4) and (5) show that a change in precipitation due to an increment in surface
 252 fluxes will exceed that due to an increment in radiative cooling. The difference of unity,
 253 nondimensionally, means that for finite and equal increments of either surface fluxes or
 254 radiative heating, the excess precipitation due to surface fluxes is equal to the increment
 255 in forcing itself.

256 Given a positive M , equation (5) states that increasing surface fluxes always increases
 257 precipitation, but precipitation responses to changes in $\langle Q_R \rangle$ can be either negative or
 258 positive in principle, depending whether M is greater or less than 1. For a small M ($M \ll$
 259 1), the difference is small. In our experiments, where M is sufficiently large (~ 0.4 , as
 260 shown below) that the difference is not negligible, surface fluxes have a significantly
 261 greater influence on precipitation than does radiative cooling.

262 The difference we see in FIG.2 is what we expect for constant M , and might have
 263 been considered a null hypothesis. It indicates no fundamental difference in how surface
 264 fluxes and radiative cooling influence the large scale circulation in these simulations. We

265 might have expected that forcing in the interior of the troposphere by radiative cooling
266 might induce differences in the thermodynamic profiles and the vertical motion profiles
267 relative to forcing at the surface by turbulent fluxes, resulting in different values of M .
268 However, the simulations here are well explained by the simplest vertically integrated
269 theory, in which M remains constant. The simulations are needed, in this sense, only to
270 provide the (single) value of M .

271 Quantitatively speaking, the slope of the rainfall in Figure 2.a (WTG, and
272 similarly for DGW) for increasing the surface fluxes, $\frac{\partial P}{\partial SF}$ is about 2.3, which
273 corresponds to $M = 0.44$ using equation (5). Similar magnitudes are obtained for $\frac{\partial P}{\partial \langle Q_R \rangle}$.
274 For DGW, however, $\frac{\partial P}{\partial SF}$ is about 3.1, and corresponds to $M = 0.32$. Both values of M are
275 close to those obtained in the control runs with $NEI = 60 \text{ Wm}^{-2}$.

276 As in Figure 3, the right hand side of (3) with constant M gives a very good estimate of
277 the changes in precipitation resulting from both types of forcings.

278

279 *2. Zero initial moisture conditions:*

280 Figure 4 is as analogous to Figure 2 but now we initialize the simulations with a
281 zero moisture profile while keeping everything else the same as above (including the
282 reference temperature profile). For WTG (Figure 4.a) the system now exhibits multiple
283 equilibria, staying in the dry state over a wide range of NEI (Sobel et al. 2007, Sessions et
284 al. 2010). Precipitation does not occur for these dry initial conditions for NEI below a

285 threshold value. Above this value, we obtain mean precipitation values identical to those
286 found with non-zero initial moisture profile for the same forcings. However, the
287 transition to a precipitating state (that is, to the apparent inability of the dry state to be
288 sustained) occurs at 60 Wm^{-2} when radiative cooling is varied, but 70 Wm^{-2} when surface
289 fluxes are varied. In other words, starting from dry conditions the system requires less
290 energy from radiation than from surface fluxes in order for precipitation to occur.

291 Under the DGW method (Figure 4.b), however, the system produces the exact
292 same precipitation rate as was produced with the non-zero initial moisture profile as an
293 initial condition. This suggests that the DGW method does not allow multiple equilibria
294 in the parameter range we have explored.

295

296 *b. Precipitation Time Series:*

297 In this section we explore whether there are any differences between the
298 influences of surface fluxes and radiative cooling in the simulations starting with dry
299 conditions other than those evident in the statistical equilibria which are eventually
300 reached. Specifically, in the simulations where precipitation eventually does occur – but
301 near the threshold value of NEI below which the dry state can be sustained – we ask
302 whether the time interval between the initial time and the time at which precipitation first
303 occurs may be different.

304 Figure 5 shows domain mean precipitation time series under WTG for the dry
305 initial conditions with NEI of (a) 70 (b) 80, and (c) 90 Wm^{-2} , all of which are near the
306 transition from existence to non-existence of the dry solution (Fig. 4a). Two points are
307 worth noticing here. First, the transition from the dry to precipitating state happens in a

308 more dramatic fashion, overshooting the statistical equilibrium value, when radiative
309 cooling is perturbed. In contrast, perturbing surface fluxes leads to a much smoother
310 transition to precipitation onset. Second, the precipitation lag due to perturbing surface
311 fluxes vs. radiative cooling is apparent, not only in the time mean picture, but also in the
312 time series, as the time interval between initialization and precipitation onset is longer for
313 a surface flux increase than an equivalent radiative heating increase. This lag decreases as
314 the NEI increases (case of 100 Wm^{-2} shows almost no lag, hence not shown).

315 In Figure 5.a, case of $\text{NEI} = 70 \text{ Wm}^{-2}$ in which precipitation occurs only from a radiative
316 cooling reduction, the onset of precipitation is delayed by about 35 days, after which it
317 takes less than 3 days to reach equilibrium.

318 The delay in precipitation onset is reduced when NEI is increased. For $\text{NEI} = 80 \text{ Wm}^{-2}$
319 (Figure 5.b), the delay is about 20 days for the radiative cooling perturbation and about
320 27 days for the surface flux perturbation. For the case of $\text{NEI} = 90 \text{ Wm}^{-2}$ (Figure 5.c),
321 delays are about 16 days and 18 days for radiative cooling and surface flux perturbations,
322 respectively.

323 The precipitation time series for the case $\text{NEI} = 40 \text{ Wm}^{-2}$ in the DGW experiment
324 with a dry initial moisture profile is shown in Figure 6. Unlike the WTG experiment, the
325 time the system takes to begin precipitating is indistinguishable for radiative cooling and
326 surface flux perturbations (the same is true for other NEI cases, not shown). This might
327 be due to the vertical structure of the large scale vertical velocity in WTG as we will
328 discuss in the next section. When starting from dry conditions, precipitation is delayed
329 for only 5 days compared to non-zero initial moisture conditions, and this lag is not
330 dependent on the NEI.

331

332 **3.2. Large Scale Vertical Velocity:**

333 We now focus on the vertical profiles of large scale vertical velocity, W . We first
334 examine these for the experiments with moist initial conditions. Time mean vertical
335 profiles of W in the precipitating equilibrium under WTG and DGW and their
336 corresponding maximum values are shown in Figures 7 and 8, respectively, for
337 experiments in which surface fluxes are perturbed. Time mean W from the experiments
338 $NEI = 0$ is not shown because it is zero by design. As expected, the large scale vertical
339 velocity is more top heavy under WTG than DGW (Romps 2012a and b; Wang et al,
340 2013). The profiles' peak values are almost identical for the same increment in radiative
341 cooling despite different precipitation magnitudes.

342 All these experiments produce moist states with non-zero precipitation (Figure 2). (Even
343 moderate rates of subsidence need not, generally, be associated with completely dry
344 states; if the condensation heating is nonzero but smaller than the radiative cooling,
345 descent will still occur.) When the NEI is negative, vertical motion is downward and
346 precipitation falls below the RCE magnitude. The opposite happens when the NEI is
347 positive.

348 The vertical structure of W also offers some clues to the precipitation onset in the
349 experiments with dry initial conditions. Figure 9 shows the time evolution of the vertical
350 structure of WTG vertical velocity for the experiments initialized with dry conditions due
351 to perturbations in (a) surface fluxes and (b) radiative cooling, for the case of $NEI = 90$
352 Wm^{-2} (other cases are similar and not shown). Consistent with the time evolution of
353 precipitation (Figure 5.c), ascending vertical motion is delayed until about the same time

354 the system precipitates. When radiative cooling is perturbed, ascending motion is strong
355 in the boundary layer at the transition time from the dry to wet state (day 16 in Figure
356 9.b). This might explain the dramatic transition in the $\langle Q_R \rangle$ perturbation experiments
357 (Figure 5).

358 One can think of radiative cooling as inhibiting convection through subsidence, which in
359 turn induces drying which keeps relative humidity low. In an atmosphere with low
360 relative humidity, convection is inhibited when entrainment mixes dry air into saturated
361 updrafts, reducing buoyancy. We hypothesize that reducing the radiative cooling is
362 quicker to eliminate the dry equilibrium than increasing surface fluxes because any
363 change in radiative cooling has an impact on humidity (and thus on the environment for
364 deep convection) throughout the troposphere, whereas the effects of surface fluxes can be
365 trapped in the planetary boundary layer if the troposphere is dry.

366

367

368 **3.3. Thermodynamic Variables:**

369

370

371 *a. Temperature anomalies:*

372 In order to induce ascending motion at any given level, mean temperature
373 anomalies, relative to the reference temperature profile, must be positive under WTG by
374 (1). This is also true, in a more approximate and vertically nonlocal sense, under DGW.
375 Figure 10 shows the time evolution of the vertical structure of potential temperature
376 anomalies (from the RCE target temperature profile) for the case of $NEI = 80 \text{ Wm}^{-2}$
377 (when surface fluxes are perturbed by 80 Wm^{-2} from the control run) initialized from the
378 dry conditions using either (a) WTG or (b) DGW method. For WTG, dry conditions are
379 maintained by colder free tropospheric temperature (negative anomalies). A transition to

380 a wet state requires positive free tropospheric temperature anomalies to generate
381 ascending motion. Such anomalies develop early in all our simulations under the DGW
382 method. Under WTG (Figure 10a), after the initialization but before precipitation onset,
383 warm anomalies build up in the lowest 1 km while cold anomalies are maintained above.
384 It appears that the buildup of low level warm anomalies contributes to greater conditional
385 instability which is eventually realized in a rapid onset of convection.

386 Unlike under WTG, the smooth vertical structure of the large scale vertical
387 velocity under the DGW method makes it more efficient at communicating temperature
388 anomalies between the boundary layer and the free troposphere, since pressure and
389 temperature adjust non-locally through the hydrostatic balance. This may explain why
390 DGW experiments appear to reach a unique statistically steady state.

391

392 *b. Relative humidity (RH):*

393 Figure 11 shows the time evolution of the vertical structure of relative humidity
394 for cases initialized with dry conditions due to perturbations in (a) surface fluxes and (b)
395 radiative cooling, with $NEI = 90 \text{ Wm}^{-2}$ (other cases are similar and not shown) in the
396 WTG experiments. The most striking feature is that for the radiative cooling
397 perturbations, there is a build-up of relative humidity exceeding 90% at approximately 2
398 km altitude, deepening the moist layer above the surface, about 5 days prior to the onset
399 of precipitation (denoted by the white dashed vertical line). This prior RH build-up does
400 not occur when surface fluxes are perturbed; in Figure 11a, the RH just above the
401 boundary layer increases substantially only after precipitation has begun, rather than
402 before as in Figure 11b. Further, the free troposphere as a whole takes a couple of days
403 after precipitation onset to moisten in Figure 11a whereas it moistens very quickly after

404 precipitation onset in Figure 11b; this suggests a more active role for free tropospheric
405 humidity in causing (or at least allowing) the onset of precipitating convection for the
406 radiative heating increase, whereas the tropospheric humidification appears to be more
407 clearly a consequence of the convection for the surface flux increase. Though a subtle
408 difference, this supports the hypothesis that radiative cooling reductions are quicker to
409 eliminate the dry equilibrium than surface flux increases because they have different
410 effects on free-tropospheric humidity in the dry equilibrium.

411 Under the DGW method, on the other hand, there is no such RH build-up (not
412 shown) when increments in either radiative heating or surface fluxes are introduced.

413

414 **3.4. Sensitivity experiments**

415

416 We have done simulations in which the initial moisture profile is neither equal to
417 the RCE profile nor zero, but different fractions of the RCE initial moisture profile. For
418 moisture profiles greater than approximately 50% of the RCE profile, only the rainy
419 equilibrium state is reached. For drier profiles, the dry equilibrium state can be reached,
420 though over a narrower range of NEI than when the completely dry initial conditions are
421 used.

422 We also have done simulations with interactive surface fluxes with specified sea
423 surface temperature. We obtain similar results to those with fixed surface fluxes if we
424 compare simulations in which the actual values of the fluxes are similar - including the
425 existence or non-existence of multiple equilibria - as long as the NEI remains in the
426 interval $(-20, 60) \text{ Wm}^{-2}$.

427 Finally, we performed ensemble simulations similar to those described here for
428 the zero moisture initial conditions but with perturbed (positive and negative)
429 temperature and wind initial conditions. Variations in precipitation onset near the
430 transition from dry to wet state are less than a day for the experiments with perturbed
431 radiative cooling, but identical in all other experiments. This indicates that the differences
432 in response are due to differences in forcing and not due to random variability.

433

434

435 **4. Conclusions**

436 Cloud Resolving Model simulations have been conducted with parameterized
437 large scale circulation to contrast the effects of surface fluxes and radiative cooling on
438 deep tropical convection. Two different parameterizations of large-scale circulation, the
439 weak temperature gradient (WTG) and damped gravity wave (DGW) methods, are used.

440 In the precipitating equilibrium state, a given change in surface fluxes induces a
441 greater change in precipitation in our simulations than does an equal change in radiative
442 heating. This difference is a straightforward consequence of the column-integrated moist
443 static energy budget with a constant normalized gross moist stability. The surface flux
444 and radiative cooling increments result in equal changes in the divergent circulation. The
445 precipitation change, however, is a consequence of both that divergent circulation change
446 and the change which would occur in its absence – that is, in radiative-convective
447 equilibrium (RCE). In RCE, surface fluxes and radiative heating have opposite effects on
448 precipitation; the overall precipitation change in our simulations is thus the sum of these

449 opposite contributions from the RCE component and equal contributions from the
450 induced circulations.

451 Aside from the differences in precipitation that result straightforwardly from their
452 different roles in RCE, however, equal increments of surface fluxes and radiative heating
453 influence our simulations identically for all practical purposes. The large-scale vertical
454 motion and moist static energy export changes induced by equal increments of the two
455 forcings are essentially identical. We might have expected, on the contrary, that the two
456 forcings would induce different responses in such a way that the normalized gross moist
457 stabilities would be different, allowing differences in large-scale vertical motion.

458 This does not occur; the gross moist stability, under both WTG and WTG, remains
459 approximately constant under each method (though it is modestly smaller under DGW
460 than WTG due to the less top-heavy vertical motion profiles). Even the small variations
461 which do occur are similar (over most of the range studied) for equal surface flux and
462 radiation perturbations. If the normalized gross moist stability were precisely constant,
463 the precipitation rate in all the experiments (under a given large-scale parameterization)
464 could be predicted accurately from the moist static energy budget (3) after doing a single
465 simulation to determine the gross moist stability, since the surface fluxes and radiative
466 cooling are both specified in these simulations. While this is a somewhat unrealistically
467 constrained situation compared to the real one in which surface fluxes and radiation are
468 interactive, it is nonetheless interesting that the one degree of freedom our simulations do
469 have in the column integrated moist static energy budget – the normalized gross moist
470 stability – is exercised almost not at all.

471 A set of simulations was also conducted in which the model was initialized with
472 zero moisture, to determine whether multiple equilibria exist and whether surface fluxes
473 and radiation affect their influence differently. Under WTG, a dry non-precipitating
474 equilibrium can be maintained over a wide range of NEI. To make a transition to a wet
475 state, the system needs a smaller increase in radiative heating than surface fluxes. We
476 interpret this as resulting from the distribution of radiative cooling through the whole
477 atmospheric column, such that reducing it reduces subsidence and increases humidity
478 above the planetary boundary layer. Consistent with this, a deepening of the moist layer
479 adjacent to the surface occurs prior to the onset of precipitation in the simulation forced
480 by a radiation change which does not occur in the simulation forced by an equal surface
481 flux change (in which the onset of precipitation occurs later).

482 In the DGW method, only a precipitating equilibrium state is found. This may be
483 understood (in the sense of proximate causes) in terms of the warm temperature
484 anomalies in the free troposphere produced by this method that cause ascending large
485 scale vertical motion.

486 Studies of self-aggregation of convection in large-domain-CRMs (Bretherton et al
487 2005; Muller and Held 2012; Jeevanjee and Romps 2013; Wing and Emanuel 2014;
488 Emanuel et al. 2014) show that interactive radiation is essential to the occurrence of self-
489 aggregation. The multiple equilibria occurring in single-column or small-domain CRM
490 simulations under WTG (e.g., Sobel et al 2007, Sessions et al. 2010) have been
491 interpreted as a manifestation of the same phenomenon, yet interactive radiation is not
492 required for its occurrence in our WTG simulations (or in those of Sessions et al. 2010).
493 Herman and Raymond (2014) show that the occurrence of multiple equilibria in WTG

494 simulations without interactive radiation is sensitive to the choice of the level used for the
495 boundary layer top, a free parameter in the method, and that multiple equilibria do not
496 occur in a new spectral WTG method which – similarly to the DGW method – is nonlocal
497 in the vertical and does not require a special treatment of the boundary layer. Their results
498 and ours appear broadly consistent, and suggest that the occurrence of multiple equilibria
499 without interactive radiation under standard WTG method may be an artifact of the
500 method’s locality in the vertical or (relatedly) its somewhat *ad hoc* treatment of the
501 boundary layer. Which (if any) of these methods produces multiple equilibria in the
502 presence of interactive radiation in CRMs, and whether the dynamics of those equilibria
503 are faithful to the dynamics of self-aggregation seen in large-domain RCE simulations,
504 remains as a question for future work.

505

506

507

508

509

510

511

512

513

514

515

516

517 **Acknowledgement**

518 This work was supported by NSF grant AGS-10088 47. We would like to acknowledge
519 high-performance computing support from Yellowstone ([ark:/85065/d7wd3xhc](https://nsls.slac.stanford.edu/ark:/85065/d7wd3xhc)) provided
520 by NCAR's Computational and Information Systems Laboratory, sponsored by the
521 National Science Foundation.

522

523

524

525

526

527

528

529

530

531

532

533

534

535

536

537

538

539

540

541

542

543

544

545

546

547

548

549

550

551

552

553

554

555

556

557

558

559

560

561

562 **References**

563 Anber, U., S., Wang, and A. H. Sobel, 2014: Response of atmospheric convection to
564 vertical wind shear: Cloud- System resolving simulations with parameterized large-scale
565 circulation. Part I: Specified radiative cooling. *J. Atmos. Sci.*, in press.

566 Blossey, P. N., C. S. Bretherton, and M. C. Wyant, 2009: Subtropical low cloud response
567 to a warmer climate in an superparameterized climate model. Part II: Column modeling
568 with a cloud resolving model, *J. Adv. Model. Earth Syst.*, 1, Art. #8, 14 pp.,
569 doi:10.3894/JAMES.2009.1.8

570 Bretherton, C. S., P. N. Blossey, and M. Khairoutdinov, 2005: An energy-balance
571 analysis of deep convective self-aggregation above uniform SST. *J. Atmos. Sci.*, 62,
572 4273–4292.

573 Chen, S. H., and W. Y. Sun 2002, A one dimensional time dependent cloud model, *J.*
574 *Meteorol. Soc. Jpn.*, 80, 99–118.

575 Edman, J., and D. M. Romps, 2014: An improved weak-pressure-gradient scheme for
576 single-column modeling, *J. Atmos. Sci.*, in press.

577 Emanuel, K., 2007: Quasi-Equilibrium Dynamics of the Tropical Atmosphere. In *The*
578 *Global Circulation of the Atmosphere*, T. Schneider and A. H. Sobel, editors, Princeton
579 University Press, 385 pp.

580 Emanuel, K., A. A. Wing, and E. M. Vincent, 2014: Radiative-Convective Instability. *J.*
581 *Adv. Model. Earth Sys.*, 6, doi: 10.1002/2013MS000270

582 Frierson, Dargan M. W., 2007: Convectively Coupled Kelvin Waves in an Idealized
583 Moist General Circulation Model. *J. Atmos. Sci.*, **64**, 2076–2090.

584 Herman, M. J., and D. J. Raymond, 2014: WTG cloud modeling with spectral
585 decomposition of heating. *J. Adv. Model. Earth Syst.* Submitted .

586 Hong, S. Y., and H. L. Pan ,1996, Nonlocal boundary layer vertical diffusion in a
587 Medium-Range Forecast model, *Mon. Weather Rev.*, 124, 2322–2339.

588 Hong, S.Y., Y. Noh, and J. Dudhia, 2006: A new vertical diffusion pack- age with an
589 explicit treatment of entrainment processes, *Mon. Weather Rev.*, 134, 2318–2341.

590 Jeevanjee, N., and D. Romps, 2013: Convective self-aggregation, cold pools, and domain
591 size, *Geophys. Res. Lett.*, 40, doi:10.1002/grl.50204.

592 Khairoutdinov, M, and K. Emanuel, 2013: Rotating radiative-convective equilibrium
593 simulated by a cloud-resolving model. *J. Adv. Model. Earth Sys.*, 5, doi:
594 10.1002/2013MS000253

595 Kim, Daehyun, Jong-Seong Kug, Adam H. Sobel, 2014: Propagating versus
596 Nonpropagating Madden–Julian Oscillation Events. *J. Climate*, 27, 111–125.

597 Klemp, J. B., J. Dudhia, and A. Hassiotis, 2008: An upper gravity wave absorbing layer
598 for NWP applications, *Mon. Weather Rev.*, 136,3987–4004.

599 Kuang, Z., 2008: Modeling the interaction between cumulus convection and linear
600 gravity waves using a limited-domain cloud system-resolving model, *J. Atmos. Sci.*, 65,
601 576–591.

602 Lin, Y.L., R. D. Farley, and H. D. Orville, 1983: Bulk parameterization of the snow field
603 in a cloud model, *J. Clim. Appl. Meteorol.*, 22, 1065–1092.

604 Ma, D., and Z. Kuang (2011), Modulation of radiative heating by the Madden-Julian
605 Oscillation and convectively coupled Kelvin waves as observed by CloudSat, *Geophys.*
606 *Res. Lett.*, 38, L21813, doi:10.1029/2011GL049734

607 Mapes, B. E., 2004: Sensitivities of cumulus ensemble rainfall in a cloud- resolving
608 model with parameterized large scale dynamics, *J. Atmos. Sci.*, 61, 2308–2317.

609 Muller, Caroline J., Isaac M. Held, 2012: Detailed Investigation of the Self-Aggregation
610 of Convection in Cloud-Resolving Simulations. *J. Atmos. Sci.*, 69, 2551–2565.

611 Noh, Y., W. G. Cheon, S. Y. Hong, and S. Raasch, 2003, Improvement of the K profile
612 model for the planetary boundary layer based on large eddy simulation data, *Boundary*
613 *Layer Meteorol.*, 107, 401–427.

614 Popke, D., B. Stevens and A. Voigt, 2012: Climate and climate change in a radiative-
615 convective equilibrium version of ECHAM6. *J. Adv. Model. Earth Syst.*,
616 doi:10.1029/2012MS000191

617 Raymond, D. J., and X. Zeng, 2000: Instability and large-scale circulations in a two-
618 column model of the tropical troposphere, *Q. J. R. Meteorol. Soc.*, 124, 3117–3135.

619 Raymond, D. J., and X. Zeng, 2005: Modelling tropical atmospheric convection in the
620 context of the weak temperature gradient approximation, *Q. J. R. Meteorol. Soc.*, 131,
621 1301–1320

622 Raymond, D. J., S. L. Sessions, A. H. Sobel, and Z. Fuchs, 2009: The mechanics of gross
623 moist stability. *J. Adv. Model. Earth Syst.*, 1, 20 pp., doi:10.3894/JAMES.2009.1.9.

624 Robe, F. R. and K. A. Emanuel, 2001: The effect of vertical wind shear on radiative-
625 convective equilibrium states. *J. Atmos. Sci.*, 58, 1427-1445.

626 Romps, D., 2012a, Numerical tests of the weak pressure gradient approximation, *J.*
627 *Atmos. Sci.*, 69, 2846–2856.

628 Romps, D., 2012b, Weak pressure gradient approximation and its analytical solutions, *J.*
629 *Atmos. Sci.*, 69, 2835–2845.

630 Rutledge, S. A., and P. V. Hobbs, 1984, The mesoscale and microscale structure and
631 organization of clouds and precipitation in midlatitude cyclones. XII: A diagnostic
632 modeling study of precipitation development in narrow cloud frontal rainbands, *J. Atmos.*
633 *Sci.*, 41, 2949–2972.

634 Sessions, S., D. J. Raymond, and A. H. Sobel, 2010: Multiple equilibria in a cloud-
635 resolving model, *J. Geophys. Res.*, 115, D12110, doi:10.1029/2009JD013376.

636 Sobel, A. H., E. D. Maloney, G. Bellon, and D. M. Frierson (2010), Surface fluxes and
637 tropical intraseasonal variability: A reassessment, *J. Adv. Model. Earth Syst.*, 2,
638 2.,doi:10.3894/JAMES.2010.2.2

639 Sobel, A. H., G. Bellon, and J. Bacmeister, 2007: Multiple equilibria in a single-column
640 model of the tropical atmosphere, *Geophys. Res. Lett.*, 34, L22804,
641 doi:10.1029/2007GL031320.

642 Tobin, I., S. Bony, and R. Roca, 2012: Observational Evidence for Relationships between
643 the Degree of Aggregation of Deep Convection, Water Vapor, Surface Fluxes, and
644 Radiation. *J. Climate*, **25**, 6885–6904.

645 Tompkins, A. M., and G. C. Craig, 1998a: Radiative–convective equilibrium in a three-
646 dimensional cloud-ensemble model. *Quart. J. Roy. Meteor. Soc.*, 124, 2073–2097.

647 Wang, S., A. H. Sobel, and Z. Kuang, 2013: Cloud-resolving simulation of TOGA-
648 COARE using parameterized large-scale dynamics, *J. Geophys. Res. Atmos.*, 118, 6290–
649 6301, doi:10.1002/jgrd.50510.

650 Wang, S., and A. H. Sobel, 2011: Response of convection to relative seasurface
651 temperature: Cloud-resolving simulations in two and three dimensions, *J. Geophys. Res.*,
652 116, D11119, doi:10.1029/2010JD015347.

653 Wing, A. A., and K. A. Emanuel, 2014: Physical mechanisms controlling self-
654 aggregation of convection in idealized numerical modeling simulations. *J. Adv. Model.*
655 *Earth Sys.*, 6, doi: 10.1002/2013MS000269.

656

657

658

659

660

661 **List of Figures**

662 FIG.1. Equilibrated vertical profiles of (a) potential temperature and (b) water vapor
663 mixing ratio from the RCE simulation.

664

665 FIG.2. Domain and time mean precipitation as a function of the net energy input (NEI) to
666 the atmospheric column for (a) WTG and (b) DGW methods using non-zero initial
667 moisture profile from the RCE experiment. The control run has $NEI = 60 \text{ Wm}^{-2}$. On the
668 red curve radiative cooling is being perturbed while surface fluxes are kept fixed at the
669 control run magnitude of 206 Wm^{-2} , while in the blue curve surface fluxes are perturbed
670 while radiative cooling is kept fixed at the control run magnitude of 145 Wm^{-2} .

671

672 FIG.3. Normalized gross moist stability (M) for the precipitating statistically steady states
673 above RCE (i.e. $NEI > 0$), using (a) WTG, and (b) DGW methods. Red symbols indicate
674 experiments with radiative cooling perturbations relative to the control run; and blue
675 symbols indicates those with surface flux perturbations.

676

677 FIG.4. Same as Figure 2 but using zero moisture initial conditions.

678

679 FIG.5. Time series of domain mean precipitation for the experiments (a) $NEI = 70 \text{ Wm}^{-2}$,
680 (b) $NEI = 80 \text{ Wm}^{-2}$, and (c) $NEI = 90 \text{ Wm}^{-2}$ using WTG method. In red are shown
681 radiative cooling perturbations and in blue surface flux perturbations relative to the
682 control run.

683

684 FIG.6. Same as Figure 5, but for the DGW method for the case $NEI = 40 \text{ Wm}^{-2}$.

685

686 FIG.7. Vertical profiles of time mean large scale vertical velocity for precipitating
687 ($NEI \neq 0$) cases $NEI = -20, 20, 40, 60, 80,$ and 100 Wm^{-2} , for a set of experiments where
688 surface fluxes are perturbed (radiative cooling perturbations produce very similar vertical
689 motion; not shown), (a) WTG, (b) DGW methods.

690

691 FIG.8. Maxima of large scale vertical velocity using (a) WTG, and (b) DGW methods as
692 a function of NEI for experiments initialized with non-zero moisture profile. In red
693 radiative cooling perturbations and in blue surface flux perturbations relative to the
694 control run.

695

696 FIG.9. Time-height contour plot of WTG large scale vertical velocity (cm/s) for cases
697 where (a) surface fluxes and (b) radiative cooling are perturbed by 90 Wm^{-2} from the
698 control magnitude (i.e. $NEI = 90 \text{ Wm}^{-2}$). Note the low-level peak of the vertical velocity
699 in case (b) by the time it starts precipitating.

700

701 FIG.10. Time-height contour plot of potential temperature anomalies (K) from the RCE
702 experiment for $NEI = 80 \text{ Wm}^{-2}$ initialized with zero moisture profile, using the (a) WTG
703 and (b) DGW method.

704

705 FIG.11. Time-height contour plot of relative humidity (%) from the WTG experiment for
706 $NEI = 90 \text{ Wm}^{-2}$, (a) surface fluxes and (b) radiative cooling being perturbed from the

707 control run. The white dashed line marks time of precipitation onset. Note the deepening
708 of the moist layer above the surface in case (b) about 5 days before precipitation. Note
709 the low RH in (a) after precipitation onset in the free troposphere as discussed in section
710 3.2.

711

712

713

714

715

716

717

718

719

720

721

722

723

724

725

726

727 TABLE 1. Control parameters of net radiation, surface fluxes and their components of
 728 sensible and latent heat flux (chosen to keep the Bowen ratio close to 0.1). The sum of
 729 surface fluxes and radiative cooling is the Net Energy Input (NEI). All the numbers are in
 730 Wm^{-2} . Bold marks the control run parameters (see text for more details on the experiment
 731 setup). NEI of 70 and 90 Wm^{-2} are for cases initialized with dry conditions using WTG
 732 method.

733

NEI	Radiative Cooling	Surface Fluxes	Latent Heat	Sensible Heat
-60	265	85	77	8
-40	245	105	96	9
-20	225	125	114	11
0	205	145	132	13
20	185	165	148	17
40	165	185	166	19
60	145	205	184	21
70	135	215	194	21
80	125	225	202	23
90	115	235	212	24
100	105	245	220	25

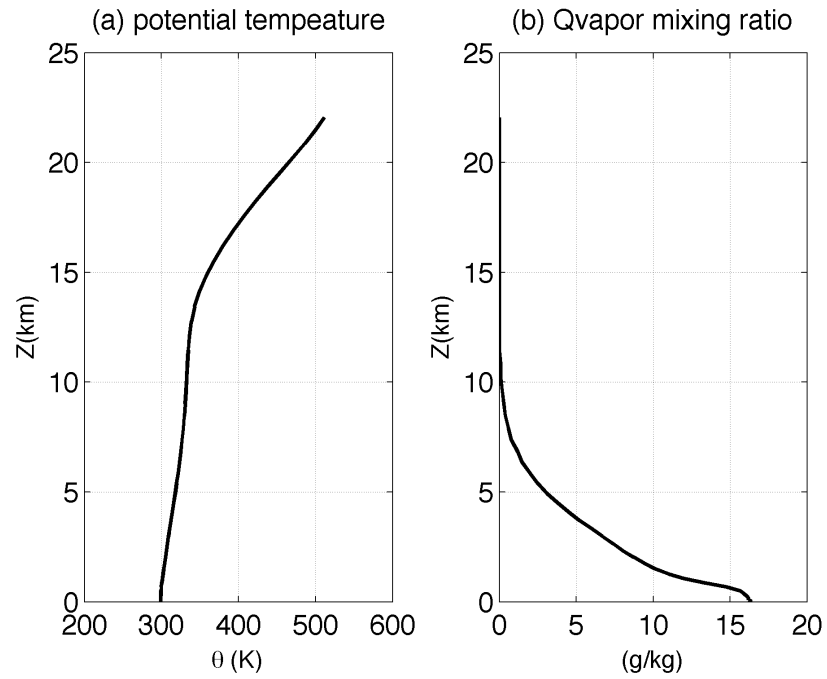
734

735

736

737

738



739

740

741 FIG.1. Equilibrated vertical profiles of (a) potential temperature and (b) water vapor

742 mixing ratio from the RCE simulation.

743

744

745

746

747

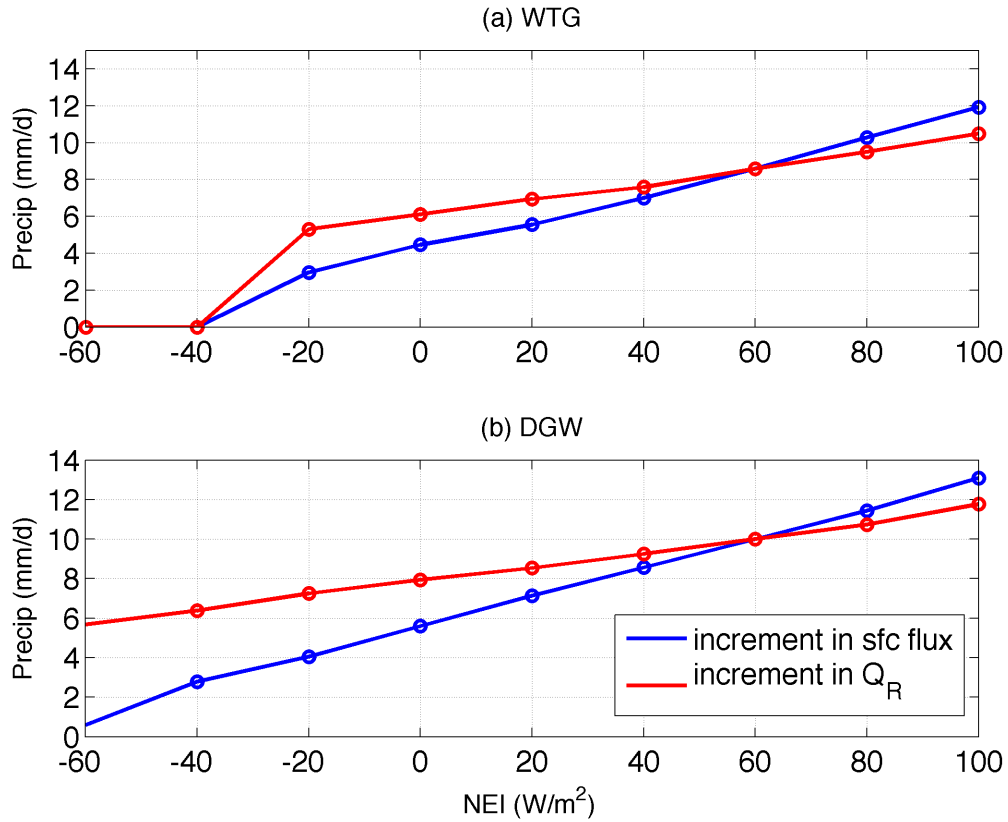
748

749

750

751

752



753

754 FIG.2. Domain and time mean precipitation as a function of the net energy input (NEI) to

755 the atmospheric column for (a) WTG and (b) DGW methods using non-zero initial

756 moisture profile from the RCE experiment. The control run has $NEI = 60 Wm^{-2}$.

757 On the red curve radiative cooling is perturbed with surface fluxes kept fixed at the control run

758 value of $206 Wm^{-2}$, while on the blue curve surface fluxes are perturbed with radiative

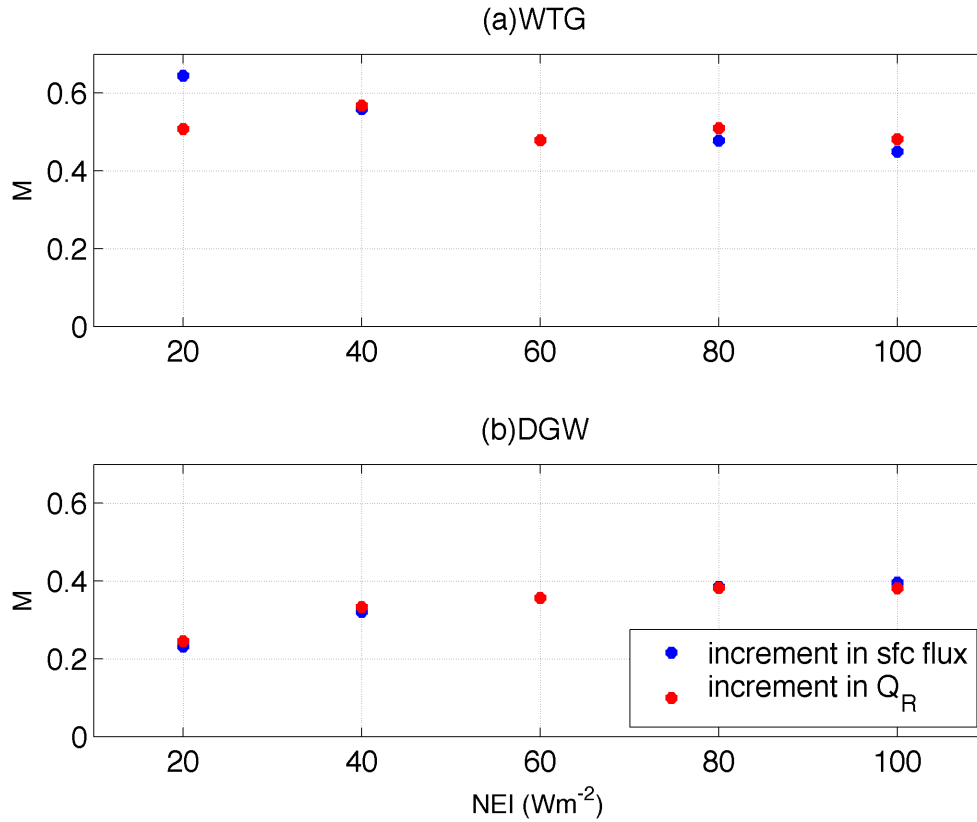
759 cooling fixed at the control run value of $145 Wm^{-2}$.

760

761

762

763



764

765

766 FIG.3. Normalized gross moist stability (M) for the precipitating statistically steady states

767 above RCE (i.e. $NEI > 0$), using (a) WTG, and (b) DGW methods. Red symbols indicate

768 experiments with radiative cooling perturbations relative to the control run; and blue

769 symbols indicate those with surface flux perturbations.

770

771

772

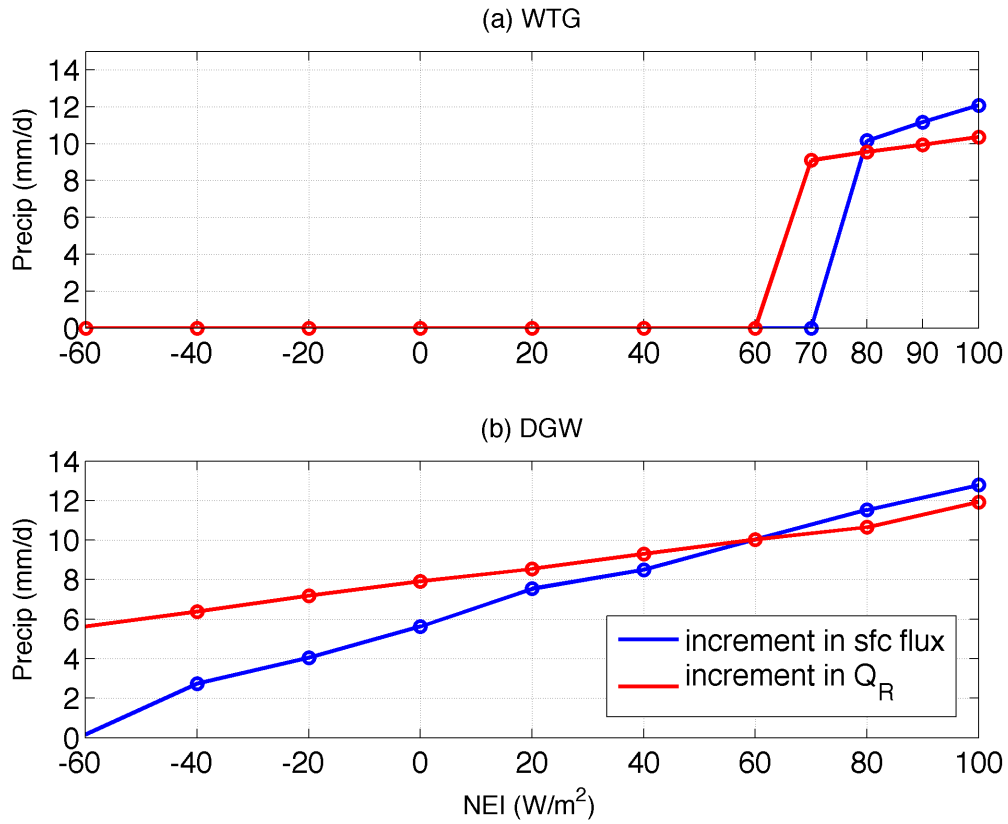
773

774

775

776

777



778

779

780 FIG.4. Same as Figure 2 but using zero moisture initial conditions.

781

782

783

784

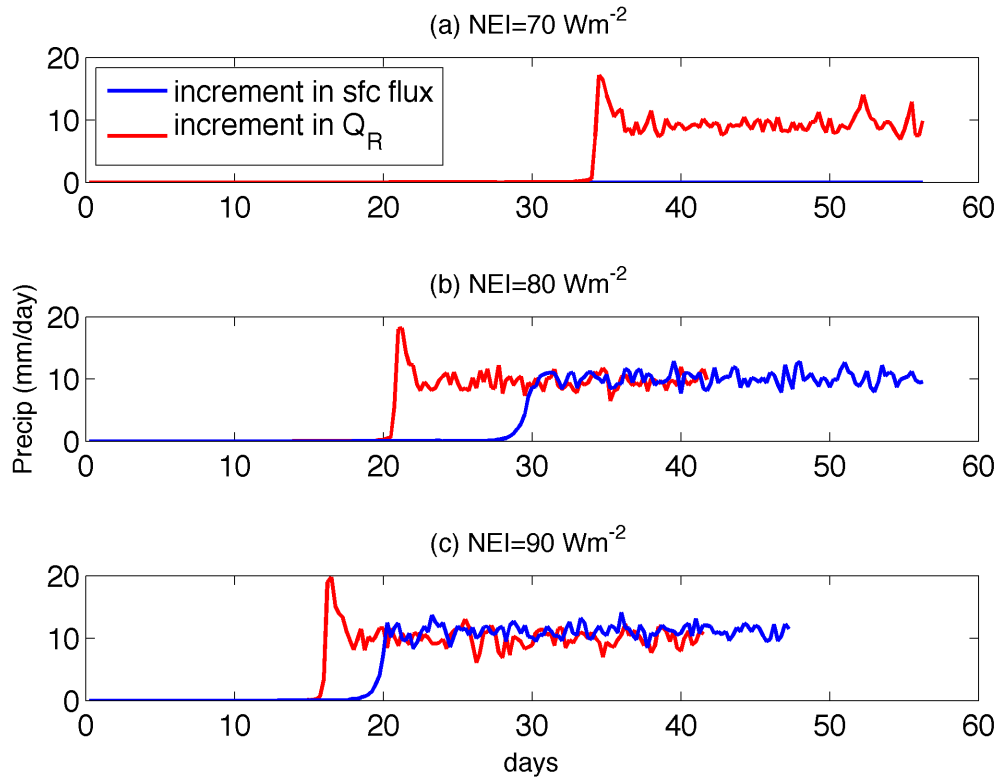
785

786

787

788

789



790

791 FIG.5. Time series of domain mean precipitation for the experiments (a) $NEI = 70 \text{ Wm}^{-2}$,

792 (b) $NEI = 80 \text{ Wm}^{-2}$, and (c) $NEI = 90 \text{ Wm}^{-2}$ using WTG method. In red are shown

793 radiative cooling perturbations and in blue surface flux perturbations relative to the

794 control run.

795

796

797

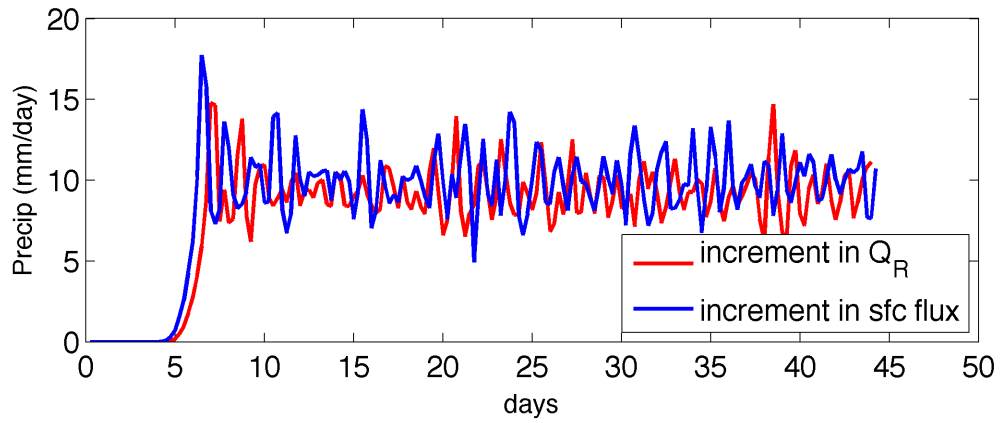
798

799

800

801

802



803

804 FIG.6. Same as Figure 5, but for the DGW method for the case $NEI = 40 \text{ Wm}^{-2}$.

805

806

807

808

809

810

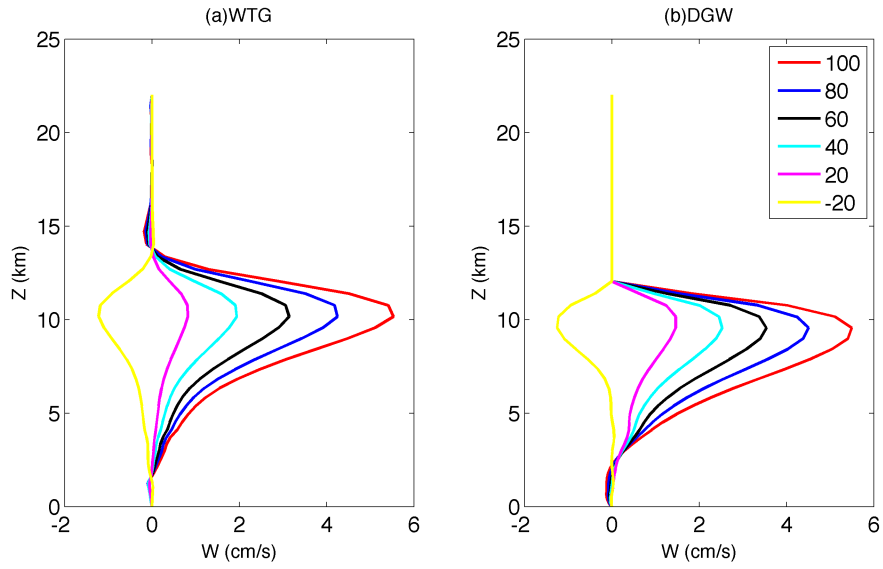
811

812

813

814

815



816

817

818 FIG.7. Vertical profiles of time mean large scale vertical velocity for precipitating
 819 ($NEI \neq 0$) cases $NEI = -20, 20, 40, 60, 80,$ and 100 Wm^{-2} , for a set of experiments where
 820 surface fluxes are perturbed (radiative cooling perturbations produce very similar vertical
 821 motion; not shown), (a) WTG, (b) DGW methods.

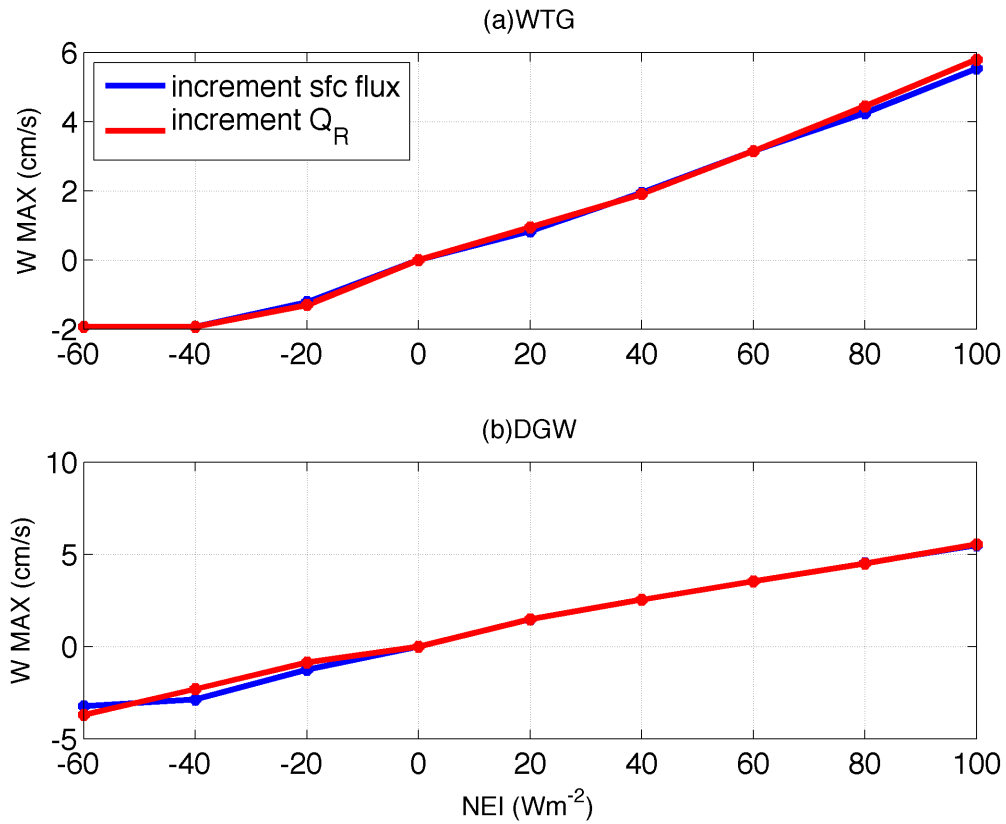
822

823

824

825

826



827

828

829 FIG.8. Maxima of large scale vertical velocity using (a) WTG, and (b) DGW methods as

830 a function of *NEI* for experiments initialized with non-zero moisture profile. In red

831 radiative cooling perturbations and in blue surface flux perturbations relative to the

832 control run.

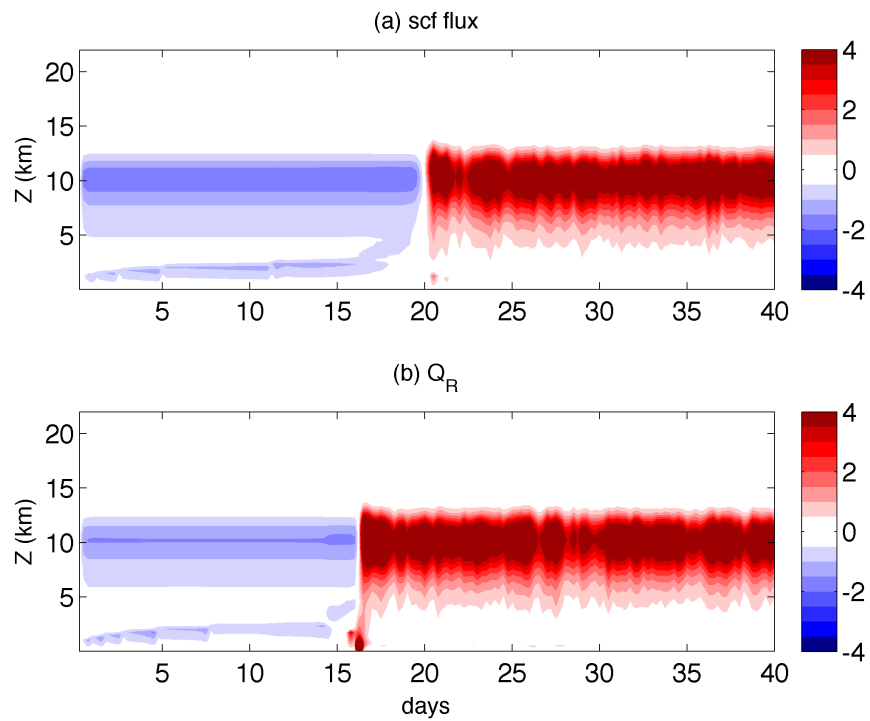
833

834

835

836

837



838

839 FIG.9. Time-height contour plot of WTG large scale vertical velocity (cm/s) for cases
 840 where (a) surface fluxes and (b) radiative cooling are perturbed by 90 Wm^{-2} from the
 841 control magnitude (i.e. $NEI= 90 \text{ Wm}^{-2}$). Note the low-level peak of the vertical velocity
 842 in case (b) by the time it starts precipitating.

843

844

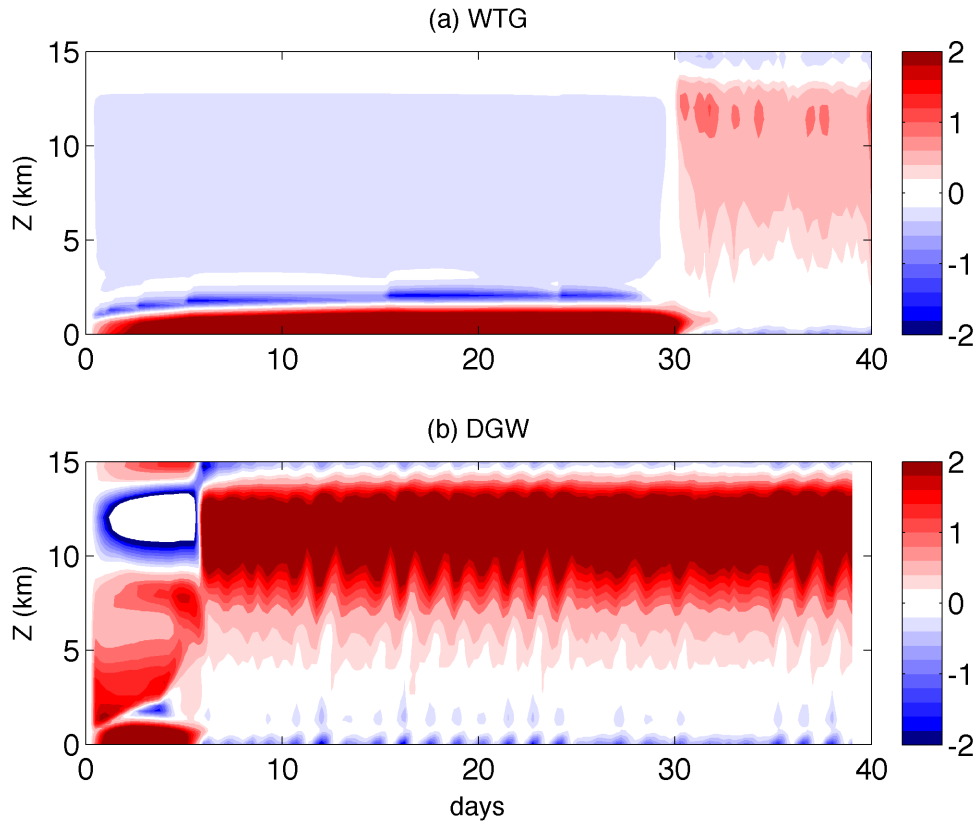
845

846

847

848

849



850

851 FIG.10. Time-height contour plot of potential temperature anomalies (K) from the RCE

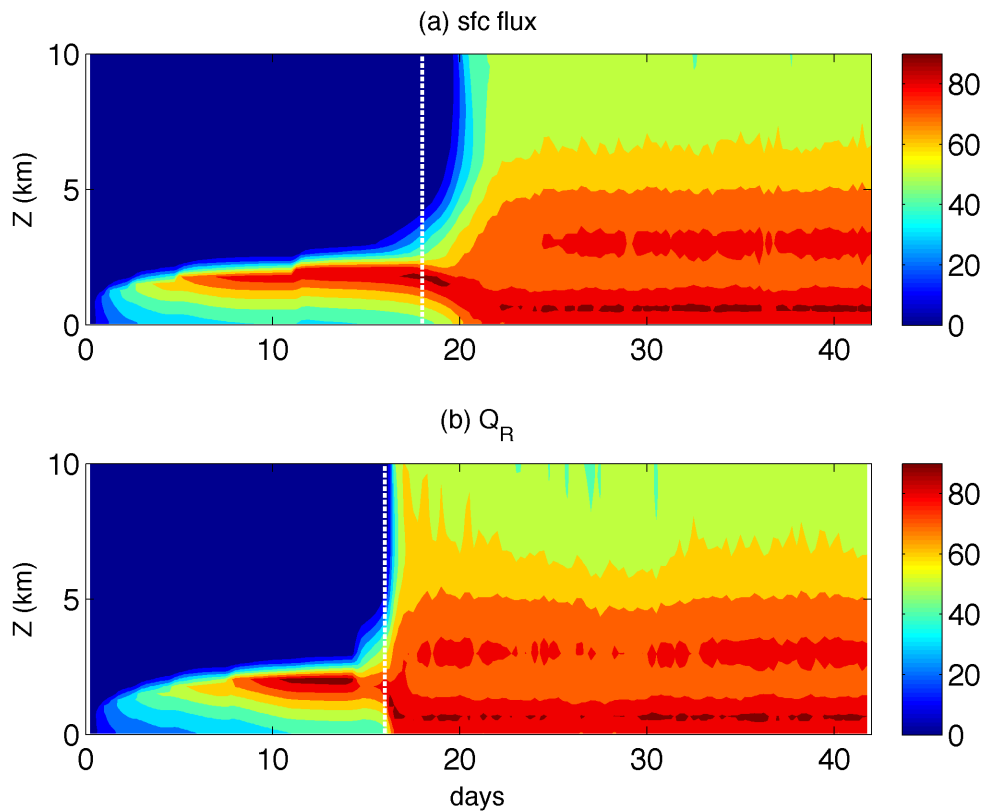
852 experiment for the $NEI = 80 \text{ Wm}^{-2}$ simulations initialized with zero moisture profile,

853 using the (a) WTG and (b) DGW method.

854

855

856



857

858 FIG.11. Time-height contour plot of relative humidity (%) from the WTG experiment for
 859 $NEI = 90 \text{ Wm}^{-2}$, (a) surface fluxes and (b) radiative cooling being perturbed from the
 860 control run. The white dashed line marks time of precipitation onset. Note the deepening
 861 of the moist layer above the surface in case (b) about 5 days before precipitation. Note
 862 the low RH in (a) 2-3 days after precipitation onset in the free troposphere as discussed in
 863 section 3.2.

864

865

866

867

868